www.springer.com/41230
https://doi.org/10.1007/s41230-022-2008-z

Solution combustion synthesis of high-entropy metal spinel oxide as oxygen evolution reaction catalyst

Tao Lu, Yue Zhang, Li Ding, Hao-yue Zheng, and *Ye Pan

School of Materials Science and Engineering, Southeast University; Jiangsu Key Laboratory of Advanced Metallic Materials, Nanjing 211189, China

Abstract: High-entropy metal spinel oxide (HEO) is proved to be a promising oxygen evolution reaction (OER) catalyst with high catalytic performance and stability. A short routine synthesis process based on solution combustion synthesis was proposed to prepare $(Co_{0.25}Ni_{0.25}Mn_{0.25}Zn_{0.25})Fe_2O_4$ spinel HEO in this work. During the process, the products were rapidly synthesized and melted due to the high-temperature reaction, and then quickly crystallized on the surface of nickel foam to form a nano-structure coating. With the aid of nano-scale spinel structure, the overpotential of non-activation HEO electrode reaches 276 mV at the current density of 10 $mA{\cdot}cm^{-2}$, and after 100 h *i-t* test, it can be further reduced to 230 mV, which proves the high activity of OER catalysis. The promotion of OER catalytic performance can be attributed to the surface reconstruction caused by the selective element leaching and the boost of oxygen vacancy, leading to the formation of nano-scale flocculation around spinel core after the long-term OER process. This work indicates a special casting process for functional materials and explores the application of rapid crystallization.

Keywords: high-entropy oxide; spinel; OER catalysis; microstructure

CLC numbers: TG146.1+6; Document code: A; Article ID: 1672-6421(2022)06-551-08

***Ye Pan**

Ph.D., Professor. His research interests mainly focus on the fabrication and properties of advanced metallic materials, solidification and microstructure controlling of metals, metallic glass and high entropy alloys, etc. To date, he has published more than 160 academic papers in international and domestic journals. He is an executive member of the Foundry Institution of Chinese Mechanical Engineering Society.

E-mail: panye@seu.edu.cn

Received: 2022-04-16
Accepted: 2022-08-23

1 Introduction

In decades, the crisis of global warming accelerates the substitution of clean energy for fossil fuels, thus the application of hydrogen is believed to be a promising candidate for the next generation of energy sources [1, 2]. Water splitting is an efficient process to produce hydrogen in the industry without hazardous byproducts. However, the anode oxygen evolution reaction (OER), which is a four-electron migration process, requires a high overpotential to form O-O bond, and thus limits the overall efficiency of reaction [3, 4]. Traditionally, noble-metal oxides are applied as OER catalysts, such as RuO_2 and IrO_2, but their high price and scarcity of resources restrict the large-scale application. Therefore, transition metal oxides are systematically explored to show a scenario of high-performance substitution of OER catalyst due to their acceptable price and earth-abundant resouces [5, 6]. Transition metal spinel oxide, which is featured by metal coordination located at both tetrahedron and octahedron, is proved to be a candidate for the substitution of noble-metal catalyst [7]. However, the investigation of transition metal spinel oxide OER catalyst was focused on the improvement of catalytic performance, little attention was paid to the promotion of catalytic stability for practical application.

Recently, high-entropy materials were explored, in which the structure of solid solution phase is stabilized by the high configuration entropy introduced by the mixing of four or five principal components with equal or near-equal atom ratios, thus they have the advantage to counter the performance decline caused by the phase transformation under severe environment [8–11]. Rost et al. [12] synthesized $(Co_{0.2}Cu_{0.2}Mg_{0.2}Ni_{0.2}Zn_{0.2})O$ high-entropy metal oxide (HEO) in rock-salt structure and found that the elevation of configuration entropy leads to the formation of single-phase structure rather than the multi-phase one

and the cation distribution in rock-salt structure is random. Dabrowa et al. [13] prepared $(CoCrFeMnNi)_3O_4$ high-entropy spinel oxide and demonstrated the material has a single-phase and solid solution structure which maybe influenced by oxygen partial pressure during the synthesis process. Then, Gild et al. [14] reported the synthesis of eight kinds of high-entropy fluorite oxide taking HfO_2, ZrO_2, and CeO_2 as principal components and TiO_2, Y_2O_3, Yb_2O_3, La_2O_3, Gd_2O_3, CaO, and MgO as phase stabilizers. These high entropy fluorites exhibit lower electrical and thermal conductivities due to high phonon scattering by multiple cations and strained lattices. Zhang et al. [15] have synthesized $(Co_{0.2}Mn_{0.2}Ni_{0.2}Fe_{0.2}Zn_{0.2})Fe_2O_4$ high-entropy spinel oxide and investigated the OER performance. The results indicated that the material shows a co-prosperity of catalytic efficiency and stability in OER performance, due to that the disordered occupation of multi-valent cations induces severe lattice distortion and elevates configurational entropy.

In this work, a facile synthesis process based on the solution combustion synthesis was designed to prepare $(Co_{0.25}Ni_{0.25}Mn_{0.25}Zn_{0.25})Fe_2O_4$ HEO electrode for OER catalysis. Solution combustion synthesis is characterized by a rapid heating and crystallization process, where the target products can be synthesized and then melted or vapored owing to the high energy produced by the chemical reaction of oxidizer and fuel. After the ignition of the reaction, the products will undergo a rapid crystallization process which can considerably limit the growth of grains. Therefore, the short routine of preparation is beneficial for the formation of high-performance OER anode electrode with the nano-scale structure of HEO spinel. The microstructure and structural reconstruction of HEO spinel during the OER process were also investigated.

2 Experimental procedures

2.1 Solution preparation

Figure 1 indicates the preparation of $(Co_{0.25}Ni_{0.25}Mn_{0.25}Zn_{0.25})Fe_2O_4$ HEO electrode via solution combustion synthesis. The reaction equation for solution combustion synthesis in this work is as follows [16]:

$$M^{v}(NO_3)_v + v\frac{5}{4}(\phi-1)O_2 + \frac{5}{9}v\phi C_2H_5NO_2$$
$$\rightarrow M_vO_{v/2} + \frac{25}{18}v\phi H_2O + v\left(\frac{5\phi+9}{18}\right)N_2 + \frac{10}{9}v\phi CO_2$$

where $M^{v}(NO_3)_v$ represents nitrates for metals Co, Fe, Mn, and Zn, respectively; v is valent of metal and ϕ is the ratio of fuel and oxidant (the value of ϕ is set to 2 for the sufficient combustion). Glycine is taken as the fuel. According to the above equation, the weighted $Co(NO_3)_2{\cdot}H_2O$, $Ni(NO_3)_2{\cdot}H_2O$, $Zn(NO_3)_2{\cdot}6H_2O$, $Mn(NO_3)_2{\cdot}4H_2O$, $Fe(NO_3)_3{\cdot}9H_2O$ and glycine (Shanghai Aladdin Bio-Chem Technology Co., Ltd.) were mixed with 10 mL deionized water in the beaker and fully stirred to get the solution. Then, the solution was dried in air for 24–48 h to form the gel ready for the reaction.

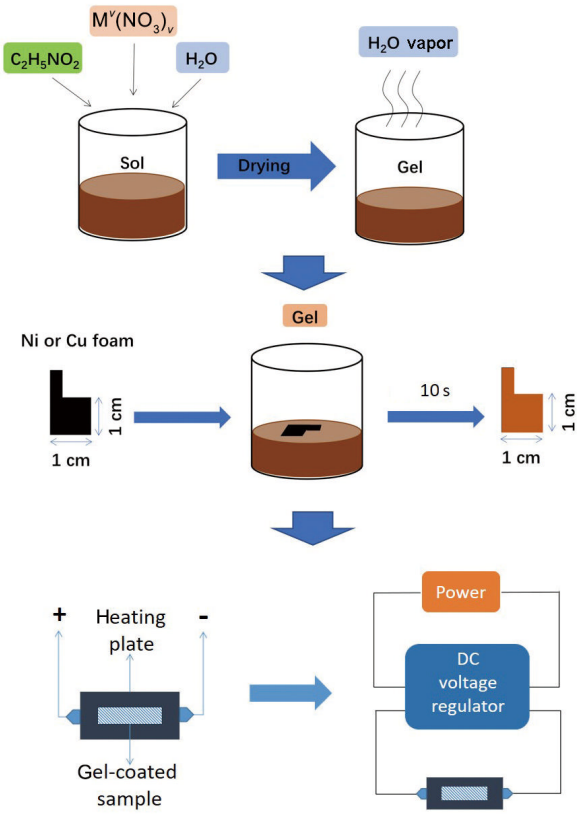

Fig. 1: Schematic of preparation of $(Co_{0.25}Ni_{0.25}Mn_{0.25}Zn_{0.25})Fe_2O_4$ HEO electrode

2.2 Electrode preparation

A foamed nickel was selected as the electrode supporter. The foam was cut into a square with a dimension of 10×10 mm^2 and an additional rectangle of 10×3 mm^2 on one side for the clamping by the electrode holder. The cut foam was moved to the gel and held for 10 s to achieve the identical dosage of reactant.

The coated foam was placed on a heating plate made of Ni-Cr alloy with a dimension of 30×10 mm^2. The heating plate was connected to a DC voltage regulator. The voltage was set to 45 V. With the power switched on, the heat was generated and transferred to the foam to ignite the reactants in a few seconds. The combustion reaction can be self-propagated after the ignition in 4–5 s. The synthesized HEO particles were crystallized on the substrate and cooled in the air to room temperature, and then the electrode was obtained.

2.3 Electrocatalysis analysis

The standard three-electrode system was employed to analyze the OER performance of high-entropy spinel catalyst, taking Ag/AgCl and Pt as the reference and counter electrodes, respectively. The electrolyte was 1 M KOH solution with a pH of 13.7. All of the electrochemical tests were performed on CHI660E workstation (CH Instruments) at room temperature. The OER overpotential was calculated by linear sweep voltammetry (LSV) at a scan rate of 5 $mV{\cdot}s^{-1}$ and was converted vs reversible hydrogen electrode (RHE) according to the equation: $E(RHE)=E(Ag/AgCl)+0.0591\times pH+0.197(V)$, where $E(RHE)$ represents OER overpotential, $E(Ag/AgCl)$

is the experimental potential taking Ag/AgCl as counter electrode, and V is the unit of potential. The Tafel slope was derived from the linear region of the LSV polarization curve and can be fitted by the Tafel equation: $\eta = b\log j + a$, where η is the OER potential of working electrode, j is the current density, b is the desired Tafel slope, and a is the intercept of Tafel curve. The exchange current density (j_0) was calculated by the extrapolation of the fitted Tafel curve.

2.4 Microstructure analysis

The crystal structure of synthesized HEO powders was analyzed by X-ray diffractometer (XRD, D8-Discover), using Cu-K radiation with a wavelength of 1.54Å and a scanning step of 0.02°. The morphology of HEO powders was explored by field emission scanning electron microscopy (SEM, FEI-3D). The microstructures were investigated by SEM and transmission electron microscopy (TEM, Tecnai G2 F30 STWIN) equipped with an energy dispersive X-ray spectrometer (EDX). X-ray photoelectron spectroscopy (XPS, Thermo ESCALAB 250XI) was employed to analyze the chemical state and elemental composition of the spinel oxides.

3 Results and discussion

Figure 2(a) presents the XRD pattern of the synthesized HEO electrode. It is obvious that the three peaks located at 45.01°, 52.24°, and 77.03°, respectively, indicate the nickel foam supporter. The magnified pattern shown in the inset depicts the peaks, located at 30.06°, 35.45°, 37.28°, 43.47°, 53.88°, 57.16°, and 62.72°, respectively, which are identical to the standard peaks of $CoFe_2O_4$ spinel (marked as the pink pattern). Thus, the XRD result confirms the formation of a single-phase spinel of $(Co_{0.25}Ni_{0.25}Mn_{0.25}Zn_{0.25})Fe_2O_4$ HEO. The morphology

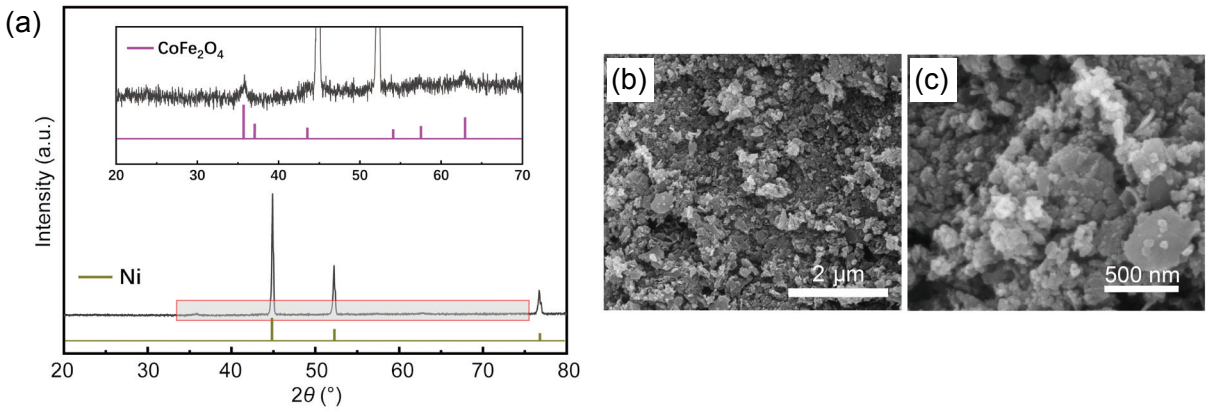

Fig. 2: XRD pattern (a) and SEM morphologies (b–c) of as-synthesized $(Co_{0.25}Ni_{0.25}Mn_{0.25}Zn_{0.25})Fe_2O_4$ HEO

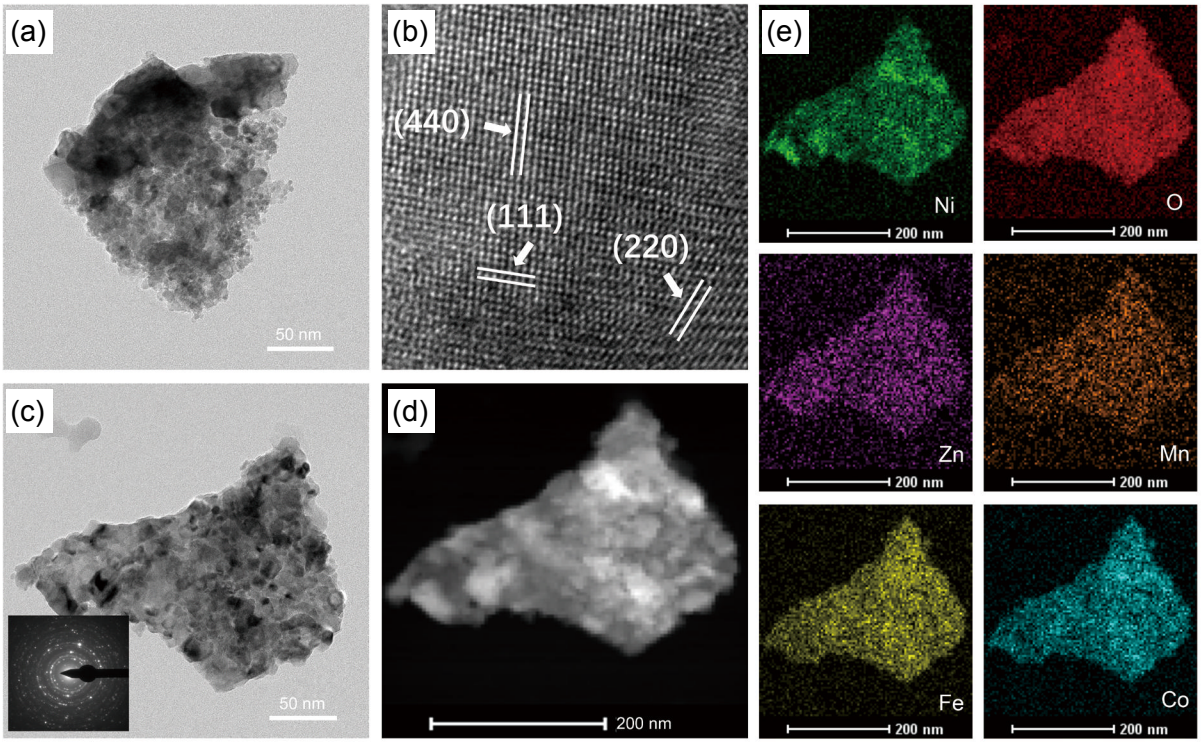

Fig. 3: TEM figures (a–c) and HAADF-HRTEM image (d–e) of as-synthesized $(Co_{0.25}Ni_{0.25}Mn_{0.25}Zn_{0.25})Fe_2O_4$ HEO

of synthesized HEO is shown in Figs. 2(b)–(c). The shapes of products are irregular, including particles, sheets and needles, etc., and all of them have a rough surface. It is clear that the products are loosely deposited on the surface of nickel foam with the dimension down to nano scale. This is contributed by the rapid cooling process after the high-temperature solution combustion which is beneficial to crystallizing nano grains and limits their accumulation. Figure 3 presents the structural characteristics and elemental analysis of synthesized HEO particles. In Fig. 3(a), it is found that the HEO particle is composed of multiple irregular nanocrystals, the size of which is 50 nm. The HRTEM image of these nanocrystals can identify the interplanar crystal spacing of 0.208 nm, 0.297 nm, and 0.486 nm, respectively, which are corresponding to (440), (220), and (111) planes of the spinel structure. The nano-multi-crystal structure of the HEO particles can also be confirmed by the selective area electron diffraction pattern shown in Fig. 3(c), which is characterized by the concentric rings. The HAADF-STEM analysis gives the elemental mapping of the HEO particle [Figs. 3(d–e)], in which the dispersion of Fe, Mn, Co, Ni, Zn, and O, respectively, is homogeneous in the particle.

Figure 4 depicts the LSV and *i-t* tests of synthesized HEO electrodes in the conditions of non-activation, cyclic voltammetry (CV)-activation and after the *i-t* test, respectively. The specific overpotential values are summarized in Table 1. It can be found that for the non-activation electrode, the overpotential at a current density of 10 mA·cm^{-2} reaches 276 mV, which is much lower than that in the similar HEO electrode prepared by the mechanical alloying as reported [15]. Meanwhile, the 100 h *i-t* test at a constant overpotential of 276 mV indicates a rise of current density from 10 mA·cm^{-2} to 24.75 mA·cm^{-2}. After the *i-t* test, the overpotential can be further reduced to 230 mV, which means promotion of OER catalytic performance. It is reported that the CV-activation

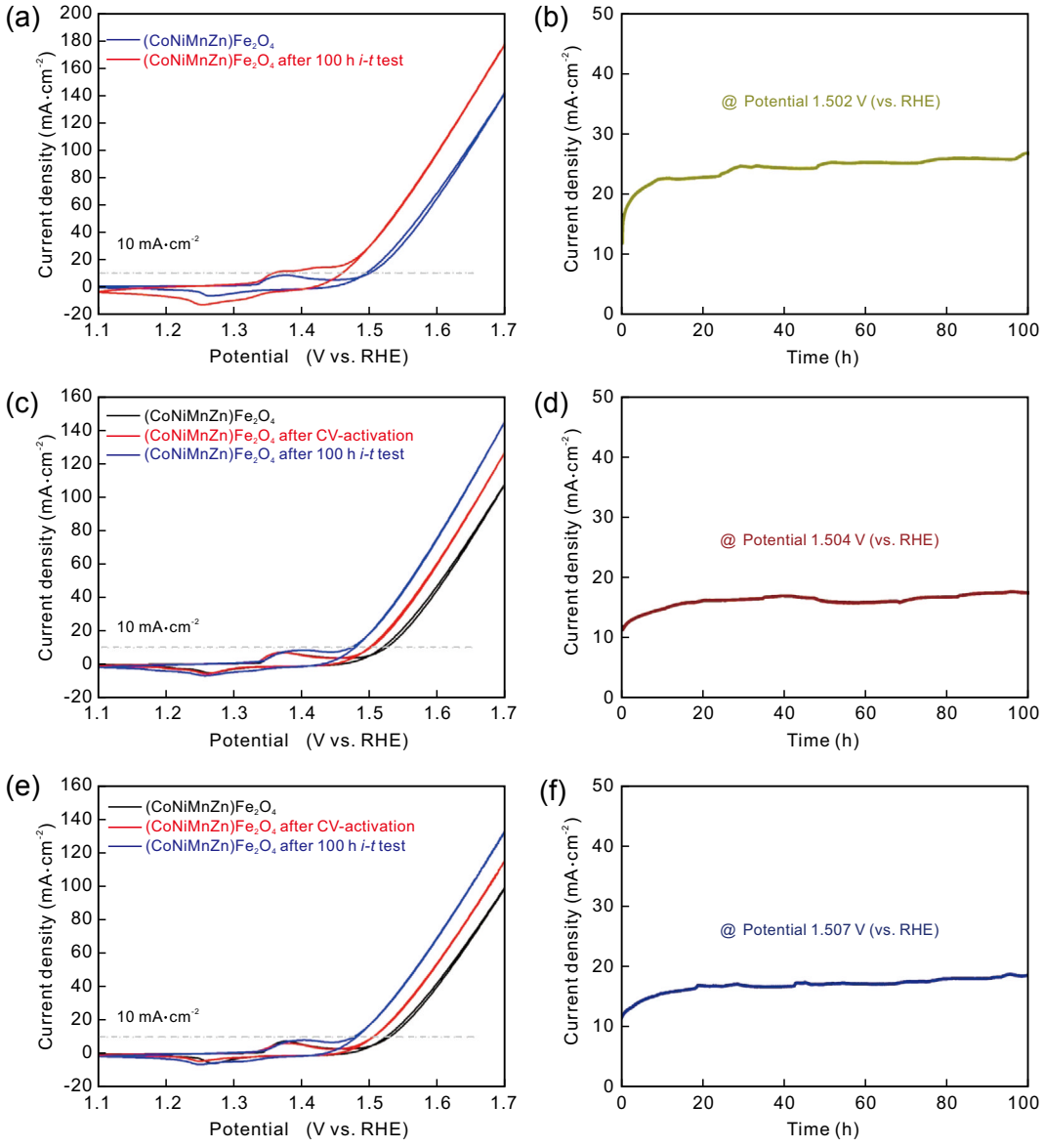

Fig. 4: LSV patterns (a, c, e) and *i-t* (b, d, f) curves of $(Co_{0.25}Ni_{0.25}Mn_{0.25}Zn_{0.25})Fe_2O_4$ HEO electrode for non-activated status (a–b), negative potential activated status (c, d) and positive potential activated status (e, f)

Table 1: OER performance of $(Co_{0.25}Ni_{0.25}Mn_{0.25}Zn_{0.25})Fe_2O_4$ HEO electrode for different status

Status	J (mA·cm^{-2})	$\eta_{original}$ (mV)	$\eta_{activated}$ (mV)	$\eta_{after\ i\text{-}t}$ (mV)
Non-activated	10	276 (±2.1)	\	230 (±2.4)
Negative potential activated	10	283 (±1.8)	274 (±1.2)	250 (±1.5)
Positive potential activated	10	280 (±2.2)	270 (±1.1)	249 (±1.2)

process can optimize the surface structure of catalyst, thus it is a critical process for high-performance catalysts [17-19]. Two kinds of CV-activated HEO electrodes were prepared employing negative potential activation (0.3–0.6 mV) and positive potential activation (0.2–0.6 mV), respectively. For the negative CV-activated HEO electrode, the overpotential is slightly reduced from 283 mV to 274 mV with the activation process. Similarly, the 100 h *i-t* test can further reduce the overpotential to 250 mV, and the current density is stabilized to 16.88 mA·cm^{-2}. The same trend of overpotential variation can be found in the positive CV-activated HEO electrode, where it is 280 mV for the raw electrode, 270 mV for the CV-activated electrode, and 249 mV after the *i-t* test, respectively. Interestingly, the CV-activation process shows the moderate effect for improving the OER catalytic performance in the synthesized HEO electrode, but a long *i-t* process can significantly motivate the catalytic process to obtain a much lower overpotential.

Figure 5 presents the surface morphologies of HEO particles obtained by CV-activation and *i-t* process, respectively. Compared to the surface of raw particles, the CV-activated particles are composed of wrinkles with dimensions down to nanoscale. Furthermore, after 100 h *i-t* test, the wrinkles on the surface become thinner and are coated by a mass of flocculation. In the magnified image of the HEO particle shown in Fig. 5(d), it is clear that the flocculation grows around the core and is finally stabilized to a certain dimension during the *i-t* test. Thus, the formation of flocculation considerably increases the active area for the OER process which can reduce the reaction barrier, so that the catalytic performance of the HEO electrode can significantly be promoted with the aid of the *i-t* process. The structure of the HEO particle after the *i-t* test is shown in Fig. 6. The core of the HEO particle maintains the spinel structure from the SAED pattern, but the flocculation around the core shows a combination of spinel and non-crystalline structure. The HAADF-STEM shows the distribution of Mn and Zn elements in the flocculation is much lower than that in the core, indicating the formation of the non-crystalline structure is due to the selective leaching of Mn and Zn on the surface.

The XPS analysis was employed to investigate the chemical bonding states of each element in the synthesized $(Co_{0.25}Ni_{0.25}Mn_{0.25}Zn_{0.25})Fe_2O_4$ HEO particle before and after the 100 h *i-t* test (Fig. 7). The spectra of transition metal elements of Co, Ni, Mn, and Fe indicate all the elements have 2+ and 3+ values, but Zn element has only 2+ value. This is identical to the status of transition metal oxides as reported in Refs. [20–22]. By comparison, it can be concluded that the binding energy of each transition metal element valence is elevated to a higher state after the 100 h *i-t* test, but the binding energy of Zn element remains the same. Thus, it is evident that the *i-t* process increases

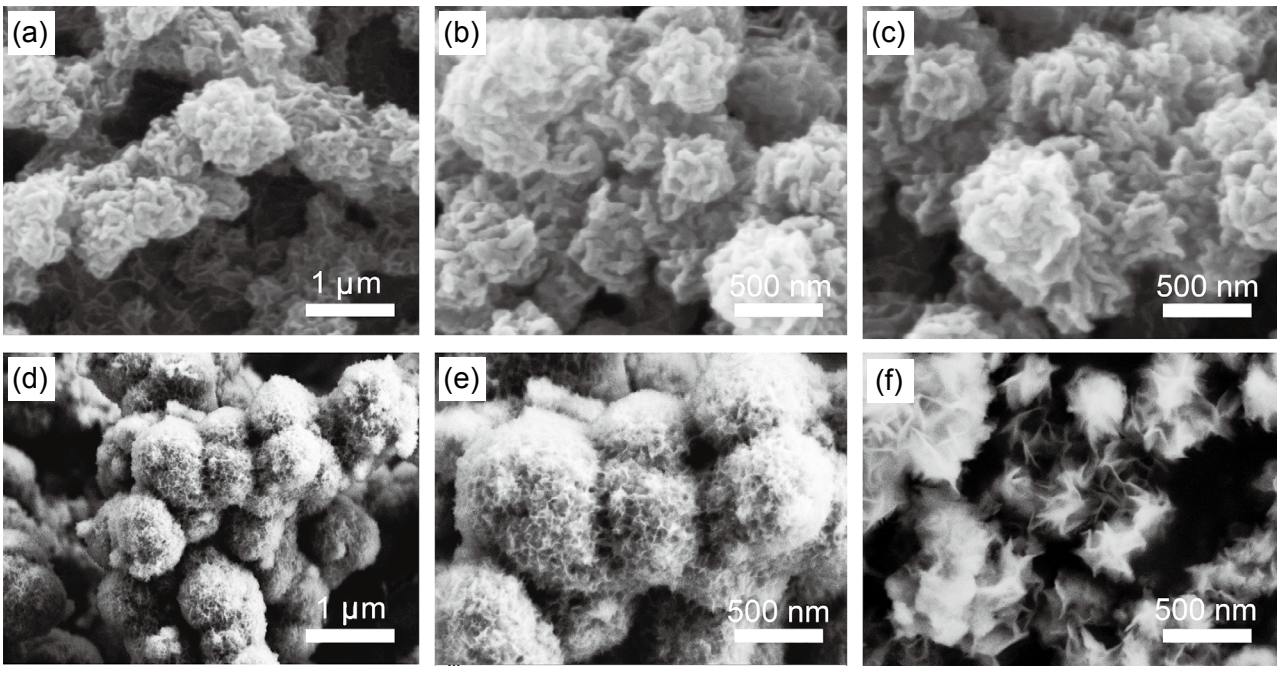

Fig. 5: SEM morphologies for $(Co_{0.25}Ni_{0.25}Mn_{0.25}Zn_{0.25})Fe_2O_4$ HEO after activation (a, b, c) and *i-t* test (d, e, f)

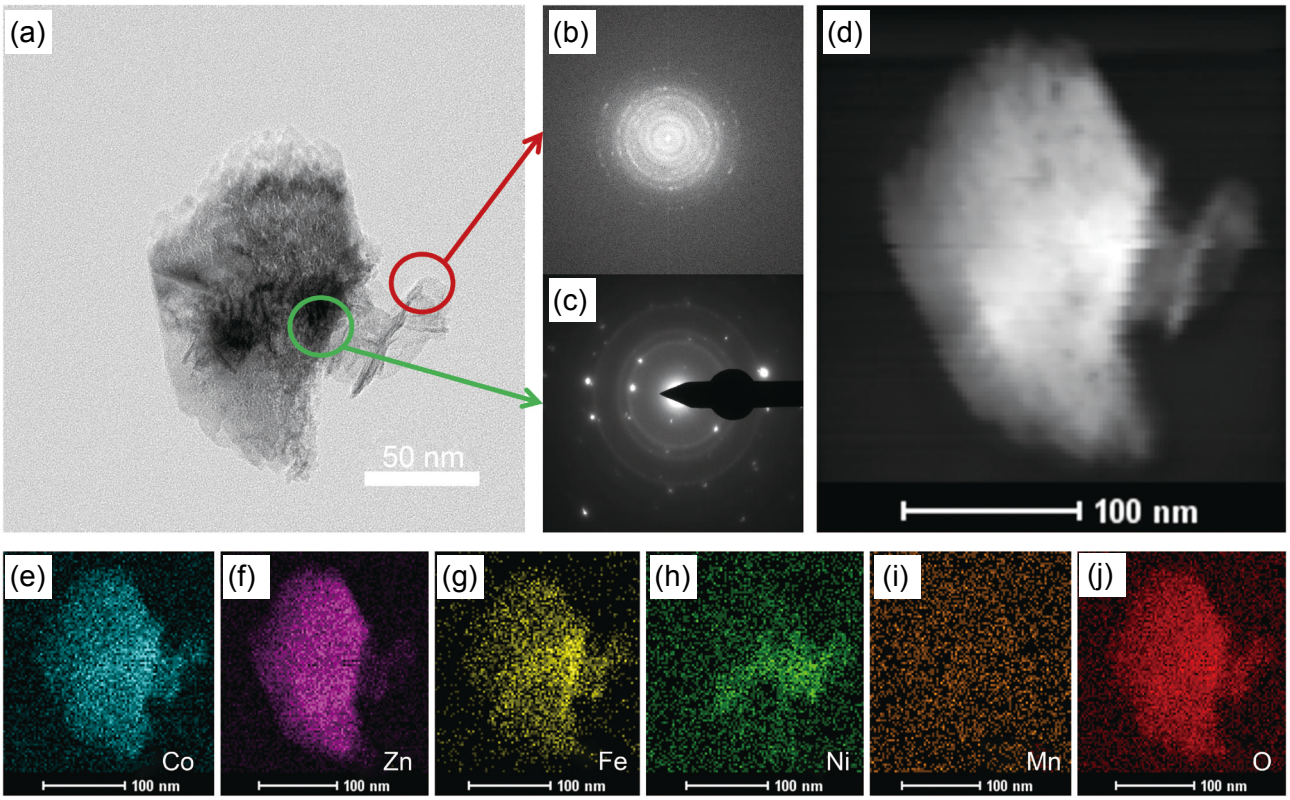

Fig. 6: TEM figures (a–c) and HAADF-HRTEM images and element distribution (d–j) of $(Co_{0.25}Ni_{0.25}Mn_{0.25}Zn_{0.25})Fe_2O_4$ HEO after *i-t* test

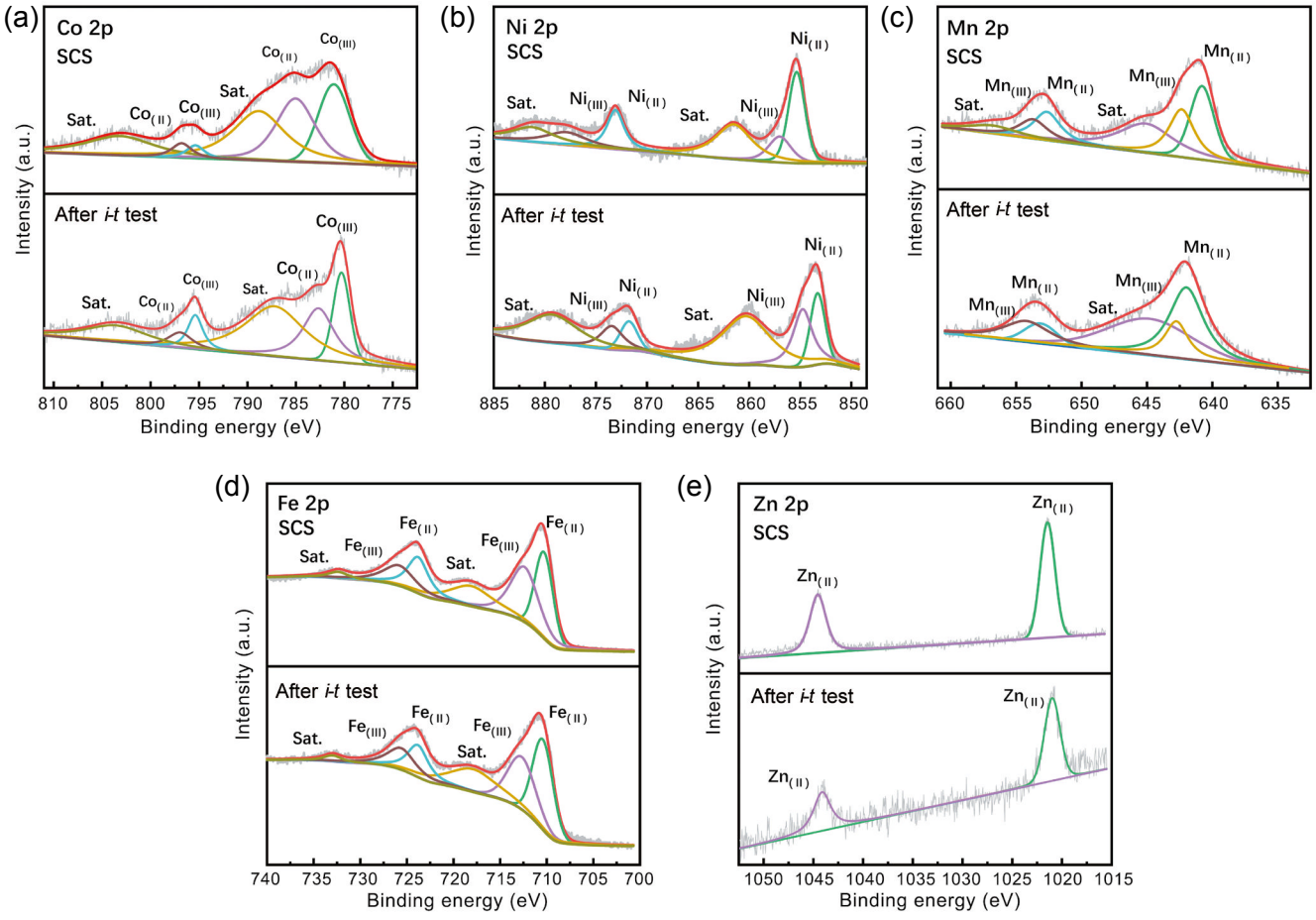

Fig. 7: XPS results for Co (a), Ni (b), Mn (c), Fe (d) and Zn (e) elements in $(Co_{0.25}Ni_{0.25}Mn_{0.25}Zn_{0.25})Fe_2O_4$ HEO before and after *i-t* test

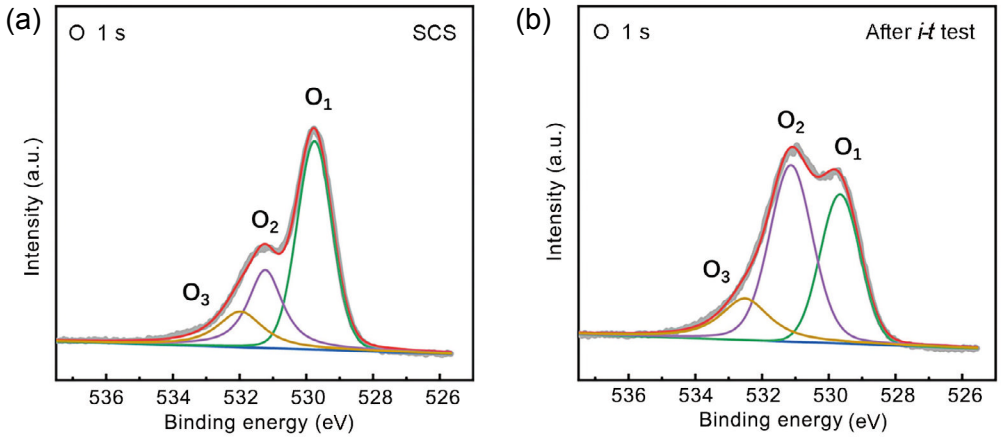

Fig. 8: XPS results for O element in $(Co_{0.25}Ni_{0.25}Mn_{0.25}Zn_{0.25})Fe_2O_4$ HEO before and after *i-t* test

the chemical binding of transition metal ions with ligand to form a stronger chemical bond. Considering the formation of the non-crystalline structure as mentioned before, the *i-t* process stimulates the structural reconstruction by means of strengthening the metal-oxygen bonds with partial leaching of Mn and Zn elements. A further observation can be found in the XPS analysis of O element shown in Fig. 8, where O_1, O_2, and O_3 peaks represent a metal-oxygen bond, oxygen vacancy, and hydroxyl oxygen or surface oxygen adsorption, respectively. After the *i-t* process, the area ratio of O_2 peak increases from 27.56% to 48.95%, meanwhile, the area ratio of O_1 peak reduces from 55.98% to 34.69%, and that of O_3 peak remains the same (16.46%). Therefore, the element leaching process is also accompanied by the formation of oxygen vacancy, so that the surface of the HEO particles cannot locally maintain the spinel structure but form the non-crystalline structure. Besides, this structural reconstruction on the surface of HEO promotes the energy of active sites which is beneficial for OER catalysis, thus it considerably reduces the reaction barrier and makes the synthesized $(Co_{0.25}Ni_{0.25}Mn_{0.25}Zn_{0.25})Fe_2O_4$ HEO particles to be a promising OER catalyst.

4 Conclusions

A solution combustion synthesis route is designed and successfully applied for the preparation of $(Co_{0.25}Ni_{0.25}Mn_{0.25}Zn_{0.25})Fe_2O_4$ HEO electrode. The high-temperature reaction facilitates the synthesis and melting of HEO products, and then the nano-grain HEO particles are crystallized on the nickel foam during the rapid cooling process. The microstructure and performance for OER catalysis were investigated. The results confirm that the application of rapid crystallization and the special casting process is a promising technology for the preparation of the functional devices. The major conclusions are drawn as follows:

(1) For the non-activation HEO electrode, the overpotential at a current density of 10 $mA \cdot cm^{-2}$ reaches 276 mV, and after the 100 h *i-t* test, the overpotential can be further reduced to 230 mV. But, the CV-activation process shows a moderate improvement in OER catalytic performance.

(2) After the *i-t* test, the core of the HEO particle maintains the spinel structure, but the flocculation around the core shows a combination of spinel and non-crystalline structure. This can be contributed to the surface reconstruction caused by the selective element leaching and the boost of oxygen vacancy.

Acknowledgements

This work was financially supported by the Research Fund of Jiangsu Key Laboratory for Advanced Metallic Materials, Southeast University (No. AMM2021A02).

References

[1] Liu Y Y, Zhou D J, Deng T Y, et al. Research progress of oxygen evolution reaction catalysts for electrochemical water splitting. Chemsuschem, 2021, 14(24): 5359–5383.
[2] Kim J S, Kim B, Kim H, et al. Recent progress on multimetal oxide catalysts for the oxygen evolution reaction. Advanced Energy Materials, 2018, 8(11): 1702774.
[3] Xiao Z H, Huang Y C, Dong C L, et al. Operando identification of the dynamic behavior of oxygen vacancy-rich Co_3O_4 for oxygen evolution reaction. Journal of the American Chemical Society, 2020, 142(28): 12087–12095.
[4] Sun S N, Sun Y M, Zhou Y, et al. Shifting oxygen charge towards octahedral metal: A way to promote water oxidation on cobalt spinel oxides. Angewandte Chemie-International Edition, 2019, 58(18): 6042–6047.
[5] Zhao Q, Yan Z H, Chen C C, et al. Spinels: Controlled preparation, oxygen reduction/evolution reaction application, and beyond. Chemical Reviews, 2017, 117(15): 10121–10211.
[6] Yang D J, Zhang L J, Yan X C, et al. Recent progress in oxygen electrocatalysts for zinc-air batteries. Small Methods, 2017, 1(12): 1700209.
[7] Wei C, Feng Z X, Scherer G G, et al. Cations in octahedral sites: A descriptor for oxygen electrocatalysis on transition-metal spinels. Advanced Materials, 2017, 29(23): 1606800.
[8] Dai W J, Lu T and Pan Y. Novel and promising electrocatalyst for oxygen evolution reaction based on MnFeCoNi high entropy alloy. Journal of Power Sources, 2019, 430: 104–111.
[9] Zhang G L, Ming K S, Kang J L, et al. High entropy alloy as a highly active and stable electrocatalyst for hydrogen evolution reaction. Electrochimica Acta, 2018, 279: 19–23.
[10] Loffler T, Meyer H, Savan A, et al. Discovery of a multinary noble metal-free oxygen reduction catalyst. Advanced Energy Materials, 2018, 8(34): 1802269.

[11] Lv Z Y, Liu X J, Jia B, et al. Development of a novel high-entropy alloy with eminent efficiency of degrading azo dye solutions. Scientific Reports, 2016, 6: 34213.
[12] Rost C M, Sachet E, Borman T, et al. Entropy-stabilized oxides. Nature Communication, 2015, 6: 8485–8493.
[13] Dabrowa J, Stygar M, Mikula A, et al. Synthesis and microstructure of the $(Co,Cr,Fe,Mn,Ni)_3O_4$ high entropy oxide characterized by spinel structure. Materials Letters, 2018, 216: 32–36.
[14] Gild J, Samiee M, Braun J L, et al. High-entropy fluorite oxides. Journal of the European Ceramic Society, 2018, 38(10): 3578–3584.
[15] Zhang Y, Lu T, Ye Y, et al. Stabilizing oxygen vacancy in entropy-engineered $CoFe_2O_4$-type catalysts for co-prosperity of efficiency and stability in an oxygen evolution reaction. ACS Applied Materials & Interfaces, 2020, 12(29): 32548–32555.
[16] Ashok A, Kumar A, Ponraj J, et al. Preparation of mesoporous/microporous $MnCo_2O_4$ and nanocubic $MnCr_2O_4$ using a single step solution combustion synthesis for bifunction oxygen electrocatalysis. Journal of the Electrochemical Society, 2020, 167(5): 054507.
[17] Peng H L, Xie Y C Z, Xie Z C, et al. Large-scale and facile synthesis of a porous high-entropy alloy CrMnFeCoNi as an efficient catalyst. Journal of Materials Chemistry A, 2020, 8(35): 18318–18326.
[18] Ma P Y, Zhao M M, Zhang L, et al. Self- supported high-entropy alloy electrocatalyst for highly efficient H-2 evolution in acid condition. Journal of Materiomics, 2020, 6(4): 736–742.
[19] Xu W, Chen H, Jie K C, et al. Entropy-driven mechanochemical synthesis of polymetallic zeolitic imidazolate frameworks for CO_2 fixation. Angewandte Chemie-International Edition, 2019, 58(15): 5018–5022.
[20] Huang Q S, Li C H, Tu Y K, et al. Spinel $CoFe_2O_4$/carbon nanotube composites as efficient bifunctional electrocatalysts for oxygen reduction and oxygen evolution reaction. Ceramics International, 2021, 47(2): 1602–1608.
[21] Wang J Y, Yang Z, Zhang M L, et al. Vertically stacked bilayer heterostructure $CoFe_2O_4$@Ni_3S_2 on a 3D nickel foam as a high-performance electrocatalyst for the oxygen evolution reaction. New Journal of Chemistry, 2020, 44(4): 1455–1462.
[22] Wang W H, Kuai L, Cao W, et al. Mass-production of mesoporous $MnCo_2O_4$ spinels with manganese (IV)- and cobalt (II)-rich surfaces for superior bifunctional oxygen electrocatalysis. Angewandte Chemie-International Edition, 2017, 56(47): 14977–14981.